ISSN 1063-7842, Technical Physics, 2014, Vol. 59, No. 1, pp. 85–92. © Pleiades Publishing, Ltd., 2014.
Original Russian Text © A.D. Pogrebnjak, M.V. Kaverin, V.M. Beresnev, 2014, published in Zhurnal Tekhnicheskoi Fiziki, 2014, Vol. 84, No. 1, pp. 86–93.

PHYSICS
OF NANOSTRUCTURES

Influence of the Phase and Elemental Compositions and Defect Structure on the Physicomechanical Properties and Tribotechnical Characteristics of Nanostructural Ti–Hf–Si–N Coatings

A. D. Pogrebnjak[a] *, M. V. Kaverin[a], and V. M. Beresnev[b]

[a] *Sumy State University, ul. Rimskogo-Korsakova 2, Sumy, 40002 Ukraine*
[b] *Kharkiv National University, pr. Svobody 4, Kharkiv, 61022 Ukraine*
**e-mail: alexp@i.ua*

Received October 23, 2012; in final form, April 16, 2013

Abstract—A new approach to preparing superhard nanostructural Ti–Hf–Si–N coatings with high physicomechanical performance is developed and tested. Samples with Ti–Hf–Si–N nanocoatings obtained under different deposition conditions were investigated using nuclear physical analysis methods, namely, Rutherford backscattering, energy-dispersive X-ray analysis, secondary-ion mass spectrometry, and the slow positron beam method, as well as by conducting X-ray diffraction analysis and microhardness measurements and testing the tribotechnical performance of the films. It is found that the grain size varies from 3.9 to 10.0 nm depending on the bias applied to the substrate and the residual pressure in the chamber during nanocoating deposition. It is shown that the microhardness varies considerably (from 37.4 to 48.6 ± 1.2 GPa) according to the percentage and number of phases, grain size, and material transfer along nanograin boundaries and interfaces. In tribological tests of the Ti–Hf–Si–N nanocoatings, the mechanism of cohesive and adhesive fracture changes and the friction coefficient may vary from 0.46 to 0.15.

DOI: 10.1134/S1063784214010149

INTRODUCTION

Nanostructural materials offer high physicomechanical properties owing to a large number of interfaces, small grain size, and the influence of the size of an intergranular layer (consisting of an amorphous or quasi-amorphous phase) [1–4]. However, some known nanostructural coatings (or films) do not satisfy such requirements as superhardness (an ultimate strength of ≥40 GPa), high thermal stability (≥1300°C), and oxidation resistance at temperatures of ≥1000°C [2]. It is therefore necessary to devise nanocomposite coatings that may satisfy the above requirements [3, 4].

This work was aimed at obtaining new nanostructural (Ti–Hf–Si)N coatings that offer a hardness of higher than 40 GPa, good thermal stability (≥1000°C), low friction coefficient, and good adhesion to a steel substrate.

EXPERIMENTAL SETUP AND TECHNIQUES FOR COATED SAMPLE INVESTIGATION

Ti–Hf–Si–N films were deposited on Steel 3 substrates with a diameter of 20 mm using a vacuum source of an HF discharge. The discharge was initiated in a vacuum chamber with a sintered Ti–Hf–Si cathode. Nitrides were obtained by supplying atomic nitrogen to the chamber at different pressures and substrate biases. The deposition parameters are listed in the table. A Bulat-3T vacuum arc source with an HF generator was used [3]. A bias was applied to the substrate from the HF pulse generator of damped oscillations at a frequency of ≤1 MHz with a pulse width of 60 μs and a pulse repetition rate of about 10 kHz. The negative self-bias of the substrate, which is due to the HF diode effect, was equal to 2–3 kV [5–7].

The elemental composition of the coatings from the first series was studied by secondary-ion mass spectrometry (SIMS) using an SAJW-0.5 SIMS mass spectrometer with a QMA-410 Balzers quadrupole mass analyzer and an SAJW-01 GP-MS glow-discharge mass spectrometer with an SRS-300 quadrupole mass analyzer (Poland, Warsaw). To gain complete information on the elemental composition, we used the Rutherford backscattering (RBS) technique with 1.3-MeV He^+ ions (the scattering angle is Q = 170°, the energy resolution of the detector is 16 keV at normal incidence of probing ions). The helium ion dose was 5 μC. The RBS spectra were processed with the standard international program package for depth

Deposition parameters of Ti–Hf–Si–N films: friction coefficient, crystallite size, and hardness for different series of samples

Series no.	Sample no.	Friction coefficient	Crystallite mean size, nm	Hf content in (HfTi) solid solution determined from the lattice constant, at %	Hardness, GPa	Nitrogen pressure in the chamber P, Pa	Substrate bias, V
1	23 (separated)	0.25–0.2	6.7	19	42.7	0.7	–200
	37 (separated)	0.3–0.6	5.0	33	48.6	0.6	–100
	31 (separated)	0.5–0.45	3.9	45	39.7	0.3	–200
2	10 (separated)	0.18–0.22	6.5	30	48.6	0.5	–180
	11 (separated)	0.15–0.26	7	28	45.4	0.7	–150
3	10 (direct)	0.5–0.45	4.0	65	37.4	0.6–0.7	–200
	35 (direct)	0.12–0.45	4.3	69	38.3	0.6–0.7	–100

profiling (the second series of the coatings). The elemental composition of the third series of the coatings was studied using another accelerator (RBS) with 1.7-MeV He^+ ions and the spectra were processed with the SIMNRA program package (Dresden, Germany) [8]. A JEOL-7000F scanning electron microscope with an energy-dispersive spectroscopy (EDS) microanalyzer (Japan) was also applied. Vacancies in the coatings were detected by means of a microbeam of slow positrons (Halle, Germany). The S-parameter was measured as a function of the incident positron energy, that is, on the depth of analysis [4, 9–12].

The mechanical characteristics of the layers were studied by nanoindentation on a Nanoindenter G200 instrument (MES Systems, United States) using a Berkovich trihedral diamond pyramid with a tip blunting radius of about 20 nm. The depth of indentation was measured accurate to ±0.04 nm. To eliminate the influence of the substrate on the measured hardness values, the nanohardness of the coated samples was measured within a depth of 200 nm. Indentations were 15 μm distant from each other. No less than five measurements were taken of each sample using a continuous stiffness measurement (CSM) device. The indentation depth was much less than one-tenth of the coating thickness [3]. Loading curves were analyzed following the Oliver–Pharr method. The X-ray diffraction (XRD) analysis of the nanostructural coatings was carried out with a DRON-4 diffractometer (St. Petersburg, Russia) and an X'Pert PANalitical diffractometer (The Netherlands) (an angular step of 0.05°, $U = 40$ kV, $I = 40$ mA, copper cathode). The morphology, structure, and elemental composition of the substrate–coating system were studied on its cross section prepared by an ion beam.

Frictional tests in the finger–surface configuration were performed with a TAU-1M tribometer under dry conditions. The friction coefficient and wear resistance of the coatings were determined at reciprocating sliding at room temperature (22 ± 1°C) and a relative humidity of 80 ± 5%. The velocity of the table with the sample was 4 mm/s, and the radius of curvature of the indenter's tip was 0.5 mm. The indenter was made of VK8 hard alloy (87.5 HRC), and the test load applied to it was 1 N.

To determine the adhesion/cohesion strength and scratch resistance, as well as to study the failure mechanism, we used a REVETEST scratch tester (CSM Instruments) [6]. The surface of the coating was scratched, under continuously rising load, by a Rockwell C-type diamond indenter with a tip radius of 200 μm. Simultaneously, the acoustic emission power, the friction coefficient, the depth of indenter penetration, and normal load F_N were recorded. Three scratches were applied on each coated sample to obtain reliable results.

The test conditions were the following: the load on the indenter grew from 0.9 to 70.0 N, the displacement rate of the indenter was 1 mm/min, the scratch length was 10 mm, the load rate was 6.91 N/min, the signal sampling frequency was 60 Hz, and the acoustic signal intensity was 9 dB.

During testing, we determined minimal (critical) load L_{C1} at which the indenter starts penetrating into the coating and load L_{C2} at which the first crack appears (cracking load). Monitoring of a fairly large number of physical parameters during tests raises the reliability of the method and the accuracy of critical load determination. The coating deformed by the diamond indenter was also examined under a built-in optical microscope and a Quanta 200 3D scanning electron microscope equipped with an integrated Pegasus 2000 system for microanalysis.

RESULTS AND DISCUSSION

Figures 1a and 1b show the energy-dispersive spectra taken of the sample with the Ti–Hf–Si–N coating (series *2*). Local analysis demonstrates the uniform distribution of elements over the thickness of the coating. This is evidenced by the results obtained with the other scanning electron microscope (Figs. 2a, 2b). Figure 2a presents the coating surface image in backscattered electrons, as well as N, Si, Ti, Fe (substrate), and Hf maps, and Fig. 2b shows the EDX spectrum with element concentrations in atomic percent. It is seen that the percentages of the elements constituting the coating are roughly equal to 13.98 (N), 33.72 (Ti), 5.04 (Si), 18.27 (Fe), and 29.00% (Hf) (series *2*).

Figures 3a and 3b shows the RBS spectra taken of these coatings (series *2*), and Figs. 4a and 4b demonstrate the depth profiles for series-*3* samples. In the subsurface layer, oxygen is observed to a depth of 15 nm; that is, an oxide film forms, which prevents the coating from further oxidation. Comparing the SIMS and RBS element profiles, one can notice some difference in the element concentrations. While the nitrogen concentration is within 40–50 at %, the titanium concentration differs more considerably. The hafnium concentration in the coating was determined at a level of 10 at % according to the RBS data and 12 at % according to the SIMS data. As to the silicon concentration, both methods give similar results [13–16]. It is well known that the RBS method is a reference method in finding heavy element concentrations and also in determining the coating thickness, since it is nondestructive. The SIMS method is more sensitive: its detection limit is as high as 10^{-6} at % for a number of elements. Unfortunately, the need for etching makes it destructive and the coating thickness determined by this method may somewhat differ from that found by RBS. Thus, combining the RBS and SIMS data with the integral information obtained by EDS, one can build a more complete picture of the depth distribution of impurities in nanostructural coatings.

It should be noted that a nanostructural material has a higher binding energy between nanograins and an intergranular quasi-amorphous layer; therefore, in these materials the work function of atoms under etching will naturally be higher than in polycrystals [1, 13]. Hence, the difference between depth profiles and/or coating thickness values obtained by the RBS and SIMS methods may vary from several percent to 10% [14, 15].

Figures 4a and 4b show the RBS profiles of elements entering into the coating (including uncontrolled impurities). These profiles are constructed without regard to the SIMS data. Comparing the RBS data (series *3*, Fig. 4b) with the EDS and SIMS data, we determined the composition of the coatings: $(Ti_{24}–Hf_{14}–Si_{12})N_{50}$ (Figs. 5a, 5b) [15, 16].

For series-*1* samples 1.000 ± 0.012 μm thick, the stoichiometric composition of the coating turned out to be $(Ti_{40}–Hf_{10}–Si_6)N_{44}$. The third series of samples with Ti–Hf–Si–N coatings was prepared by changing the bias to –200 V and the chamber pressure to 0.7 Pa [17, 18].

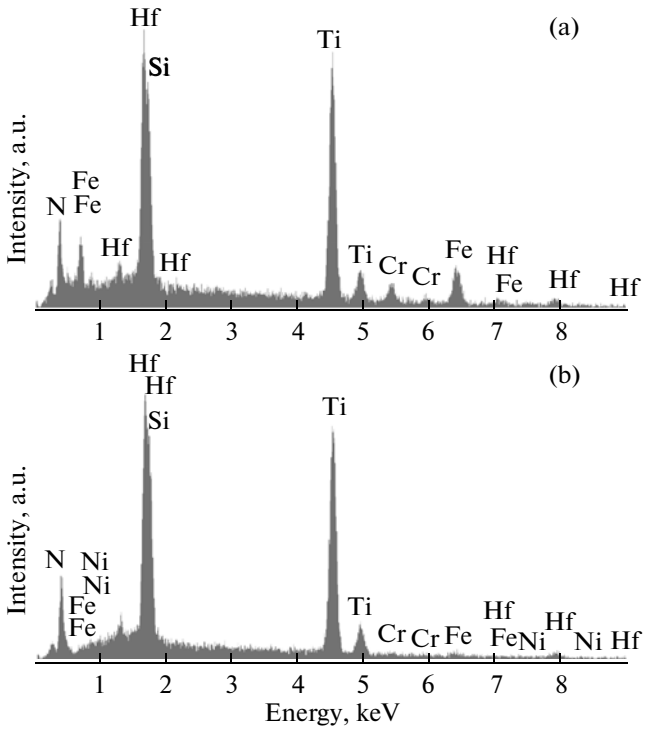

Fig. 1. Energy-dispersive spectra of the samples coated by Ti–Hf–Si–N films: (a) integral information from a 2 × 2-mm area and (b) local analysis (series *1*).

The stoichiometric composition of the coating from the second series of samples is shown in Fig. 2b. It is seen that here the element concentration ratio in the coating differs significantly from those in series-*1* and series-*3* samples (Figs. 3a, 3b; Figs. 4a, 4b). While in series-*1* and series-*3* coatings, the concentration of the constituents differs insignificantly (for Hf, the difference is 10.8 at %; for Si, 6.5 at %; etc.), the concentration of titanium in series-*2* samples is lower, that of hafnium is about 29 at %, and the concentration of nitrogen is also almost 2.5 times lower.

Figure 6 plots the *S*-parameter against the energy of the incident positron microbeam. The depth vacancy profiles shown in this figure (series-*2* and series-*3*) differ considerably from each other both in stoichiometry and in phase composition (Figs. 3a, 3b). That is, in one case, we have a two-phase system consisting of α-Si_3N_4 and (Ti, Hf)N, as is distinctly seen in Fig. 6, where the curves run in a quite different manner. Exactly the two-phase coating has two peaks (increase in the *S*-parameter): first near 10 keV and then at 20 keV (near the substrate–coating interface). In the other case, the one-phase system of (Ti, Hf)N solid solution, the *S*-parameter is rather high, 0.492,

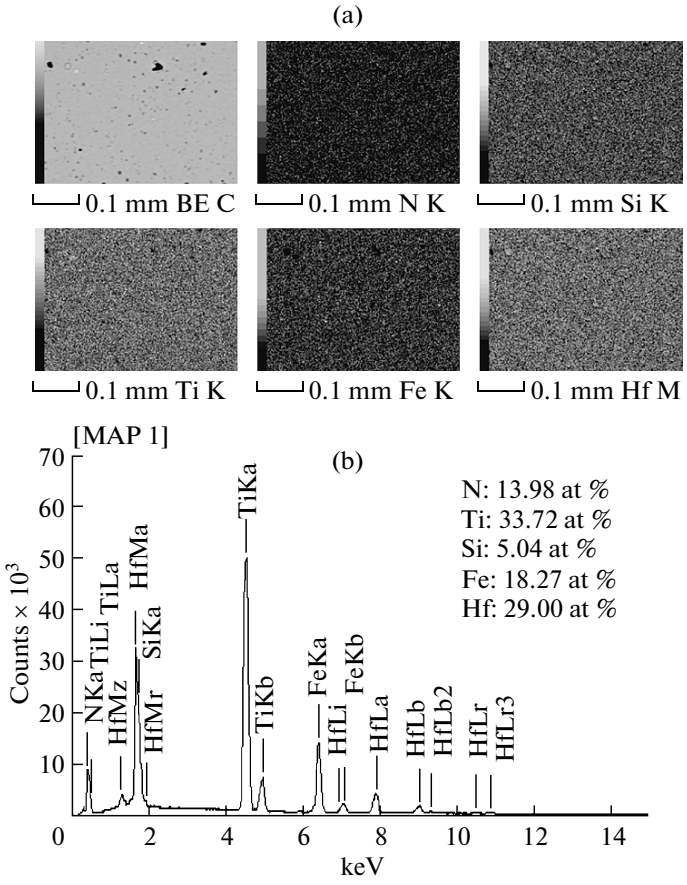

Fig. 2. Images obtained under the JEOL-7000F scanning electron microscope: (a) surface of the coating in backscattered electrons and (b) N, Si, Ti, Fe (substrate), and Hf maps in elemental contrast (series *2*).

and goes down to 0.476 near the substrate–coating interface [9–12].

From the figures corresponding to the application of the positron beam it follows that when the coating is two-phase, consisting of (Ti, Hf)N solid solution and the α-Si_3N_4 quasi-amorphous phase, positrons annihilate, that is, are trapped by nanopores at the interfaces, since the size of nanograins in (Ti, Hf)N varies from 3.9 to 10.0 nm and those in the quasi-amorphous phase (consisting of one or two monolayers), from 0.8 to 1.2 nm [4]. Therefore, the volume fraction of interfaces will reach 30–50% of the volume fraction of the entire coating [3].

Before we proceed with the analysis of the XRD data, we note that it is necessary to compare the heats of formation of possible nitrides to gain an insight into processes in the subsurface layer that are attendant on deposition. According to [5], $\Delta H298(\text{HfN}) = -369.3$ kJ/mol, $\Delta H298(\text{TiN}) = -336.6$ kJ/mol, and $\Delta H298(Si_3N_4) = -738.1$ kJ/mol. That is, the heat of formation of all the systems is relatively high and negative, indicating the high probability of forming such systems at every stage of material transfer from the target to the substrate. The heats of formation of TiN and HfN are seen to be close to each other, which favors the formation of fairly uniform (Ti, Hf)N solid solution.

XRD analysis actually revealed the formation of exactly this two-phase system (all diffraction peaks of this system lie between the peaks of TiN (JCPDS 38-1420) and HfN (JCPDS 33-0592)). This system was identified as substitutional solid solution (Ti, Hf)N, and weak diffuse peaks in the angular interval $2\theta = 40°–60°$ seem to be the peaks of the second phase α-Si_3N_4 (Fig. 7, curve *3*).

The formation conditions of nanocomposite Ti–Hf–Si–N coatings lead to a considerable distortion of the grain lattice, and hence, generate compressive stresses in the coating. Strains in the crystal lattice of the samples can be determined from diffraction patterns obtained by separating the ion–plasma flux (Fig. 7; curves *1*, *2;* series *2*). In this case, we superimposed lines obtained under oblique illumination (in taking spectra) and found that mean strain $\langle\Sigma\rangle = -1.9\%$ for sample no. 10 (lattice parameter $a = 0.4305$ nm, curve *1*) and $\langle\Sigma\rangle = -1.6\%$ for sample no. 11 ($a = 0.4303$ nm, curve *2*).

From the XRD analysis data it follows that the structural features of the coatings obtained from the

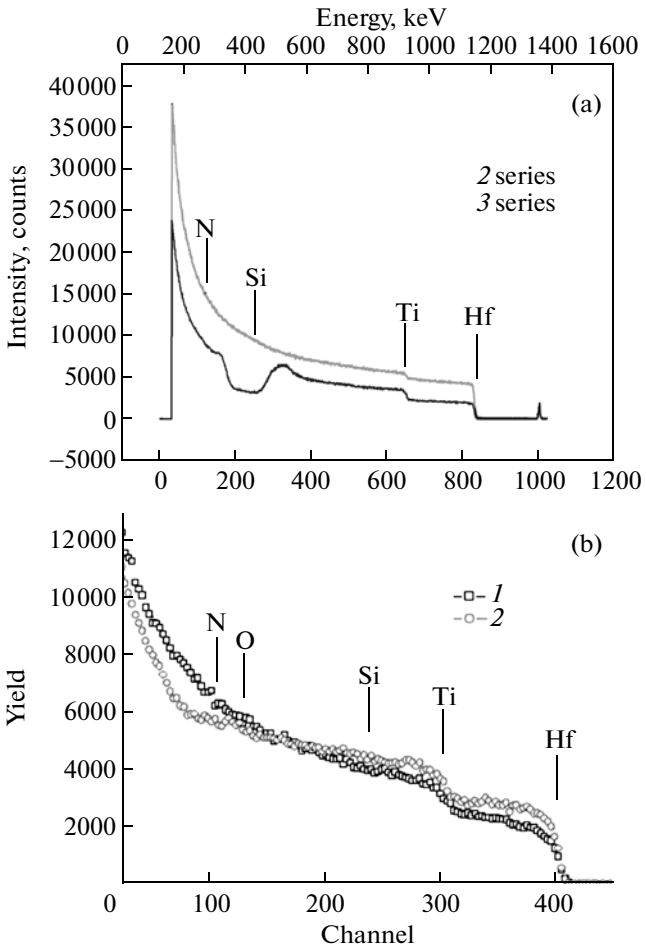

Fig. 3. Energy spectrum of backscattered 1.3-MeV He^+ ions taken from the steel substrate covered by the Ti–Hf–Si–N film for three series of samples.

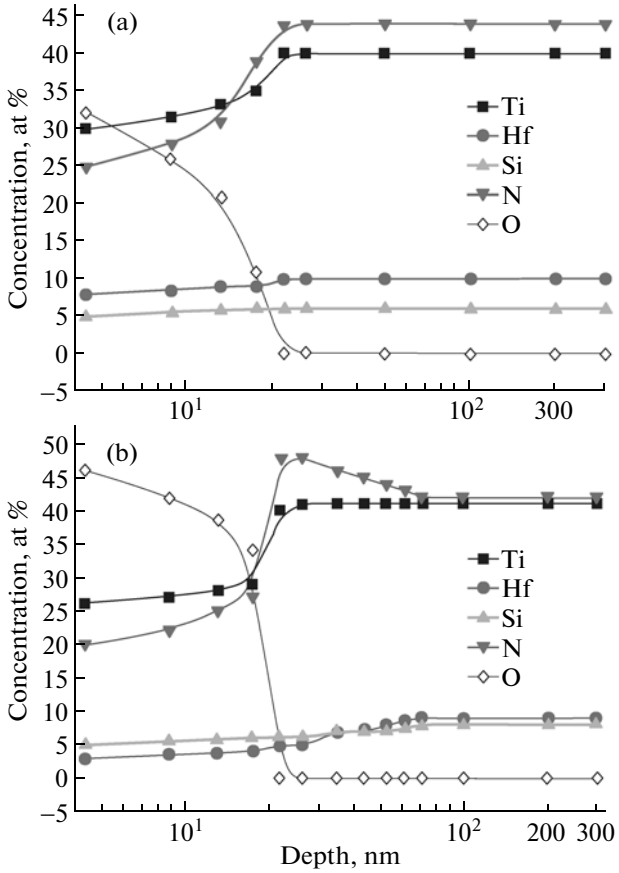

Fig. 4. (a) RBS profiles of the Ti–Hf–Si–N coating elements (including uncontrolled impurities) and (b) depth distribution of the elements derived from the RBS spectra with regard to the fact that the atomic density of the layer is close to the atomic density of titanium nitride (series *2*).

same target differ greatly according to whether the beam was separated or unseparated (direct). The respective results are given in the table.

Figure 7 shows that when the plasma flow is direct (unseparated), nontextured polycrystalline coatings with rather intense peaks are deposited. Intense peaks indicate that, with the coating thicknesses being comparable, the solid solution contains a higher concentration of Hf, which has a higher reflectivity compared with Ti.

In the case of the separated beam, the deposited coatings are to a different extent textured. When the substrate bias is not high (–100 V), we observe a [110] texture. In this case, the coating consists of textured and nontextured crystallites. The volume percentage of textured crystallites is about 40%, and their lattice parameter is larger than in nontexturted ones. The most plausible reason for such a difference is the nonuniform distribution of Hf atoms in the coating, namely, they seem to occupy mostly lattice sites in textured crystallites. Texturing increases the crystallite mean size in the direction of film-forming particle incidence (in the direction normal to the growth surface). For example, the mean size of nontextured crystallites is 6.7 nm, while in textured ones, it is considerably larger, 10.6 nm. Such coatings offer the highest nanohardness (see the table).

When the bias voltage is increased to –200 V and separation is used, the crystallite mean size in the deposited coatings decreases to 5 nm and the volume percentage of textured crystallites sharply drops (to about 20 vol %). In this case, the axis of texture is oriented in the [001] direction. It should also be noted that when the bias rises from –100 to –200 V (i.e., the energy of the plasma flow increases), the amount of textured crystallites grows and a lattice with the same value of the space charge forms [19, 20].

However, the lattice constant in this case, 0.4337 nm, is larger than that of nontextured crystallites, which arise when a low bias voltage is applied to the substrate. According to Vegard's law for solid solutions, this value of the lattice constant corresponds

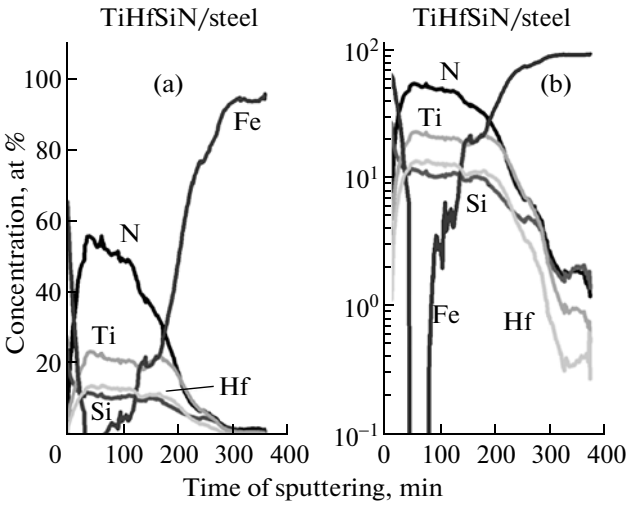

Fig. 5. SIMS profiles of the elements in the Ti–Hf–Si–N film for their following concentrations: 24% Ti, 10% Hf, 12% Si, and 54% N: (a) normal concentration scale (in atomic percent) and (b) logarithmic scale (series *2*).

to 33 at % Hf in the (Hf, Ti) metallic solid solution of the nitride phase (in calculations, we used the tabulated values of the lattice constants: 0.424173 nm for TiN (JCPDS 38-1420) and 0.452534 nm for HfN (JCPDS 33-0592).

It is known that compressive stresses in the coating decrease the angle of the diffraction peak in the θ–2θ configuration and calculation overestimates the lattice constant, that is, the hafnium concentration in the solid solution (the error may reach 5–10 at %). Therefore, from our calculation data, we can only judge the upper limit of the Hf concentration in the solid solution. The above calculations were made for samples obtained when the pressure in the working chamber during deposition was equal to 0.6–0.7 Pa. With the pressure reduced to 0.3 Pa (such conditions were realized in the case of separation at a bias voltage of –200 V, sample no. 31, series *1*), the percentage of heavy Hf atoms in the coatings grows. In addition, when the pressure decreases, so does the mean size of crystallites. The attendant effects can be associated with an increasing role of the radiation factor with decreasing working pressure. Indeed, the decrease in the working pressure is expected to be accompanied by a decrease in the probability of energy loss by atoms through collisions in the substrate–target gap. Thus, film-forming atoms, being rather energetic, favor secondary sputtering on the substrate and induce radiation defects. The former effect raises the relative Hf concentration in the coating; the latter increases the number of nuclei and, accordingly, decreases the crystallite mean size in the coating. In the coatings obtained at a pressure of 0.6–0.7 Pa in the absence of beam separation (direct-flow conditions), the lattice constant is higher because of an increased number of Hf atoms in them (see the table) [7]. It seems that the more vigorous direct-flow deposition conditions make crystallites finer because of an increased nucleus formation rate. In addition, the decrease in the crystallite size becomes more pronounced when a high bias voltage (–200 V) is applied. This seems to be natural, since the enhancement of the radiation factor causes the dispersion of the structure [8].

Figure 8 shows test data obtained on the REVETEST scratch tester for sample no. 23 at minimal (critical) load $L_{C1} = 2.46$ N and cracking load $L_{C2} = 10.25$ N.

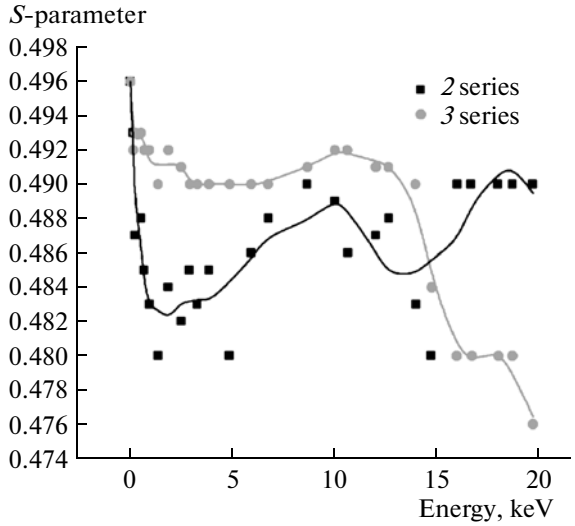

Fig. 6. *S*-parameter vs. the energy of the incident positron microbeam for three series of the samples.

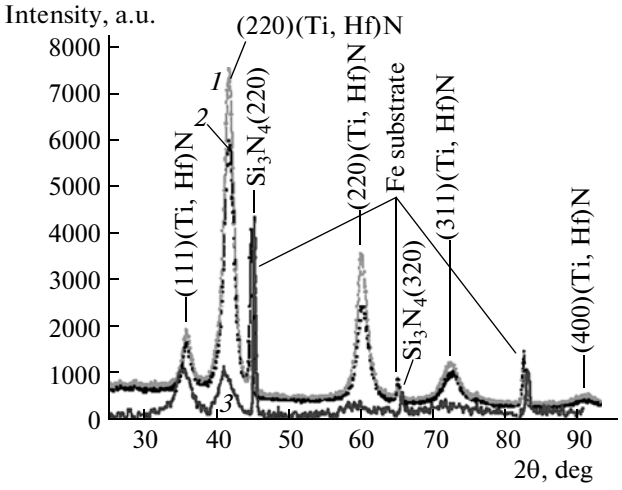

Fig. 7. Diffraction spectra taken of the Ti–Hf–Si–N coatings for samples from two series: (*1*) sample no. 10 (series *2*), (*2*) sample no. 11 (series *2*), and (*3*) sample no. 28 (series *3*).

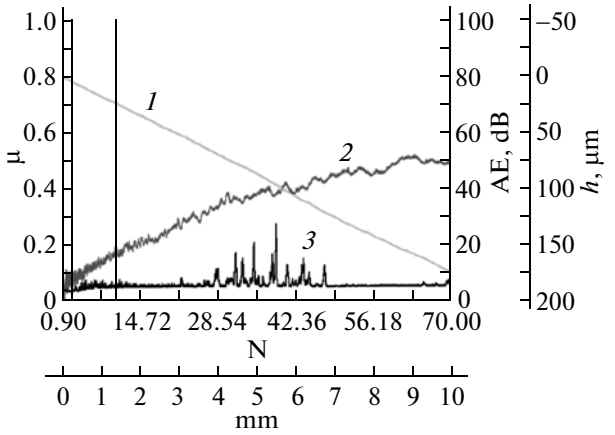

Fig. 8. Results of tests carried out on the REVETEST scratch tester for sample no. 23 (series *1*): (*1*) penetration depth h, (*2*) friction coefficient μ, and (*3*) acoustic emission (AE) intensity.

It should be noted that as the load grows, the friction coefficient-versus-load curve starts oscillating: with an increase in the friction coefficient, the acoustic emission intensity exhibits a spike and the indenter penetrates into the material more slowly. From the behavior of all the parameters studied, it follows that a hard coating more than 1 μm thick covering a softer material furnishes significant resistance to a diamond indenter up to its complete wear-out under high loads [19, 21].

When testing coatings, one can readily distinguish different threshold loads causing different types of fracture and only minimal (critical) load L_{C1} and cracking load L_{C2} can be related to adhesive damages of the coatings.

Damage starts with the appearance of chevron cracks on the bottom of a wear slot, which contributes to local stresses and friction forces and thereby results in rapid wear of the coating [22–24].

From the results of adhesion tests, the cohesive fracture of sample no. 23 starts at minimal (critical) load $L_{C1} = 2.38$ N and adhesive fracture (plastic wear) starts at $L_{C2} = 9.81$ N.

The friction coefficient of sample no. 35 at the early stage equals 0.12. Then, after 2.5 m of motion, the friction wear of the coating takes place (cracks and depressions are observed). The friction coefficient grows to 0.45, suggesting that the coating is not very hard. In the case of coated sample no. 23, the friction coefficient increases to 0.25 because of the very high roughness of the coating. Then, at the stage of steady wear, it equals 0.2. The friction coefficient, acoustic emission intensity, and indenter penetration depth were studied in detail on all the samples.

CONCLUSIONS

Thus, it was shown that when the bias voltage varies, so does the stoichiometric composition of the coating and either two phases, namely, (Ti, Hf)N solid solution and an α-Si_3N_4 quasi-amorphous phase, or one phase (solid solution) appear in the condensed (deposited) coating. Two-phase nanocomposite coatings obtained by cathode vacuum arc deposition offer a better hardness, high tribological characteristics, and good adhesion to the substrate. The hardness of one-phase nanocomposite coatings is somewhat lower, whereas their thermal stability and oxidation resistance are considerably higher (as follows from preliminary test data). The respective critical temperatures exceed 1000°C. For comparison: harder two-phase coatings oxidize intensely at 900°C.

ACKNOWLEDGMENTS

This work was supported by the Ministry of Education and Science, Youth, and Sports of Ukraine in the framework of a state program (order no. 411), by the State Foundation for Fundamental Research of Ukraine (project no. 041/20), by the Ministry of Science and Education of the Russian Federation (State Contract no. 16.552.11.7004), and partially by scientific project no. 011U001382 "Formation of Superhard Nanostructural Multicomponent Coatings with High Physicomechanical Properties."

Investigations were conducted in cooperation with the National Institute of Material Science (Tsukuba, Japan), Martin-Luther Universitat (Halle-Wittenberg, Germany), and Ion Beam Center HZDR (Dresden, Germany).

The authors thank O.V. Sobol', V.V. Uglov, D.A. Kolesnikov, P. Konarsky, K. Oyoshi, Y. Takeda, G. Abrasonis, and R. Krause-Rehberg for assistance in experiments.

REFERENCES

1. A. D. Pogrebnjak, A. G. Ponomarev, A. P. Shpak, and Yu. A. Kunitskii, Phys. Usp. **55**, 270 (2012).
2. J. Musil, J. Vlcek, and P. Zeman, Adv. Appl. Ceram. **107**, 148 (2008).
3. A. D. Pogrebnyak, A. P. Shpak, N. A. Azarenkov, and V. M. Beresnev, Phys. Usp. **52**, 29 (2009).
4. R. F. Zhang, A. S. Argon, and S. Veprek, Phys. Rev. **79**, 245 (2009).
5. W. F. Gale and T. C. Totemeier, *Smithells Metals Reference Book* (Butterworth–Heinemann, Oxford, 1976).
6. A. D. Pogrebnjak, O. V. Sobol, and V. M. Beresnev, Nanostruct. Mater. Nanotechnol. IV: Ceram. Eng. Sci. Proc. **31**, 127 (2010).
7. A. D. Pogrebnjak, Sh. M. Ruzimov, D. L. Alotseva, et al., Vacuum **81**, 1243 (2007).
8. Simnra.com

9. A. D. Pogrebnyak, A. G. Ponomarev, D. A. Kolesnikov, V. M. Beresnev, F. F. Komarov, S. S. Mel'nik, and M. V. Kaverin, Tech. Phys. Lett. **38**, 623 (2012).
10. R. Krause-Rehberg and H. S. Leipner, *Positron Annihilation in Semiconductors* (Springer, Berlin, 1999).
11. V. I. Grafutin, O. V. Ilyukhina, G. G. Myasishcheva, E. P. Prokop'ev, S. P. Timoshenkov, Yu. V. Funtikov, and R. Burtsl, Yad. Fiz. **72**, 1730 (2009).
12. J. Kansy, Mater. Sci. Forum **652**, 363 (2001).
13. V. I. Grafutin and E. P. Prokop'ev, Phys. Usp. **45**, 59 (2002).
14. A. D. Pogrebnjak, A. P. Shpak, V. M. Beresnev, et al., J. Nanosci. Nanotechnol. **12**, 9213 (2012).
15. P. Konarski, I. Iwanejko, A. Mierzejewska, and R. Diduszko, Vacuum **63**, 679 (2001).
16. P. Konarski, I. Iwanejko, and A. Mierzejewska, Appl. Surf. Sci. **203–204**, 757 (2003).
17. A. D. Pogrebnjak, V. M. Beresnev, A. A. Demianenko, V. S. Baidak, F. F. Komarov, M. V. Kaverin, N. A. Makhmudov, and D. A. Kolesnikov, Phys. Solid State **54**, 1882 (2012).
18. A. D. Pogrebnyak, A. P. Shpak, V. M. Beresnev, G. V. Kirik, D. A. Kolesnikov, F. F. Komarov, P. Konarski, N. A. Makhmudov, M. V. Kaverin, and V. V. Grudnitskii, Tech. Phys. Lett. **37**, 637 (2011).
19. A. D. Pogrebnjak, M. M. Danilionok, V. V. Uglov, N. K. Erdybaeva, G. V. Kirik, V. S. Rusakov, A. P. Shypylenko, P. V. Zukovski, and Yu. Zh. Tuleushev, Vacuum **83**, 235 (2009).
20. A. V. Khomenko and I. A. Lyashenko, J. Frict. Wear **31**, 308 (2010).
21. A. D. Pogrebnyak, A. A. Drobyshevskaya, V. M. Beresnev, M. K. Kylyshkanov, G. V. Kirik, S. N. Dub, F. F. Komarov, A. P. Shipilenko, and Yu. Zh. Tuleushev, Tech. Phys. **56**, 1023 (2011).
22. A. V. Khomenko and N. V. Prodanov, Carbon **48**, 1234 (2010).
23. A. N. Valyaev, V. S. Ladysev, D. R. Mendygaliev, A. D. Pogrebnjak, A. A. Valyaev, and N. A. Pogrebnjak, Nucl. Instrum. Methods Phys. Res. B **171**, 481 (2000).
24. A. G. Ponomarev, V. I. Miroshnichenko, and V. E. Storizhko, Nucl. Instrum. Meth. Phys. Res. A **506**, 20 (2003).

Translated by V. Isaakayn